Journal of Crystal Growth 634 (2024) 127675

Contents lists available at ScienceDirect

Journal of Crystal Growth

journal homepage: www.elsevier.com/locate/jcrysgro

# Gas effects on horizontal ribbon growth

Nojan Bagheri-Sadeghi, Brian T. Helenbrook *

*Department of Mechanical & Aerospace Engineering, Clarkson University, Potsdam, NY 13699-5725, United States*

ARTICLE INFO

Communicated by C.W. Lan

*Keywords:*
A1 Computer simulation
A1 Heat transfer
A1 Fluid flows
A1 Interfaces
A2 Growth from melt
B2 Semiconducting silicon

ABSTRACT

Three-phase (solid, melt, and gas) and two-phase (solid and melt) models of horizontal ribbon growth were compared to identify the significance of different gas effects. The boundary conditions at the melt–gas and solid–gas interfaces for two-phase simulations were obtained from decoupled simulations of the gas phase. The results showed that the gas shear stress strongly changes the flow and temperature fields and the position of the triple-phase line. Also, the gas pressure distribution determined the vertical position of the triple-phase line. In the absence of growth angle effects, the results of the two-phase model with specified convective heat transfer coefficient, shear stress, and pressure as boundary conditions along the gas phase interface closely matched that of the three-phase model. Even with non-zero growth angle effects, the two-phase model with all the boundary conditions agreed well with three-phase simulation results, despite increased deviations at higher pull speeds. Finally, the results indicated that gas-induced velocities are significant compared to the Marangoni and buoyancy velocities, which could lead to flow instabilities and the variations in solid shape as observed in HRG experiments.

## 1. Introduction

In processes of crystal growth from a melt like Czochralski (CZ), floating zone (FZ), and horizontal ribbon growth (HRG) the solid and melt are often surrounded by a gas. Three-phase simulations of such processes are challenging due to complexities at the melt–gas interface or the triple-phase line where the three phases meet. Thus, two-phase models are used where the gas effects (i.e. energy, mass, and momentum transfer due to the gas) are included as boundary conditions.

In CZ and FZ, radiation is the dominant heat flux and thus the convective heat transfer due to the gas is usually neglected in two-phase models of CZ [1–4] or FZ [5–8]. Still, some two-phase simulations of CZ include a constant convective heat transfer coefficient for gas [9,10]. For high-pressure systems, however, three-phase models of CZ [11,12] and FZ [13] show that the heat and momentum transfer due to the gas can significantly modify the convection inside the melt and the melt–gas interface shape and dynamics. Furthermore, three-phase simulations of unconventional CZ systems with a high-velocity gas flowing near the solidification zone show that the gas shear stress can modify the melt convection [14]. Finally, the gas can transfer species in such solidification systems. For instance, Bornside et al. [15] used a two-phase model of CZ to obtain the temperature distribution along the gas phase boundaries. Next, using the temperature distribution as boundary conditions, they simulated the gas phase separately to determine the transport of carbon through the inert gas from graphite parts to the melt and solid silicon.

In HRG of silicon, as first proposed by Kudo [16], convection by a cold helium jet provides the main heat flux for removing the latent heat of fusion. In their two-phase model of HRG, Daggolu et al. [17–19] used a constant convective heat transfer coefficient, which was estimated from experimental results of [16]. Helenbrook et al. [20] decoupled the gas effects by simulating the helium jet separately and then using the obtained heat flux distribution as a boundary condition in their two-phase simulations. The same approach was used in several subsequent studies [21–28]. However, this approach neglects the effects of the shear stress and pressure of the gas.

The main purpose of this paper is to demonstrate the importance of different gas effects in HRG. This is achieved by comparing two-phase and three-phase simulations of HRG. The two-phase models were created by extending the work of Helenbrook et al. [20] extracting the convective heat transfer coefficient, shear stress, and pressure from decoupled gas phase simulations. Three-phase flow fields from HRG are presented for the first time. Comparing the two-phase and three-phase results allows an improved two-phase model of the process to be developed.

* Corresponding author.
*E-mail address:* bhelenbr@clarkson.edu (B.T. Helenbrook).

https://doi.org/10.1016/j.jcrysgro.2024.127675
Received 3 January 2024; Received in revised form 14 March 2024; Accepted 19 March 2024
Available online 22 March 2024

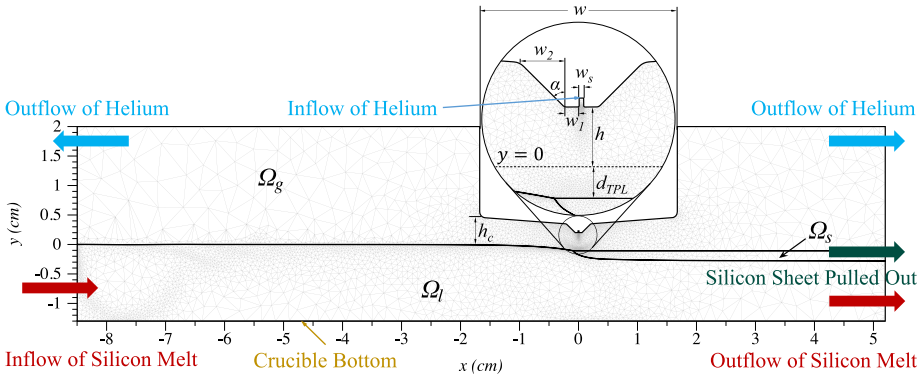


**Fig. 1.** Schematic and a sample mesh. The circular inset is a zoomed-in view near the helium jet inlet. The helium jet exits from the slot with width $w_s$. The numerical resolution is 4 times finer than the mesh shown as fourth-degree basis functions were used.

## 2. Methods

### 2.1. Three-phase model

The three-phase model for the HRG of silicon, first detailed in [29] was used. Fig. 1 shows the geometry and a sample mesh with solid, liquid, and gas subdomains designated as $\Omega_s$, $\Omega_l$, and $\Omega_g$. The solid was assumed to be a rigid body moving horizontally at the pull speed, $u_p$. The cooling helium jet slot had a width of $w_s = 0.15$ mm and was centered at $x = 0$. A slot inlet section of length $2w_s$ was simulated to allow natural evolution of the jet exit. The melt–gas interface at the inlet is fixed at $y = 0$ whereas the solid–gas interface evolves to reach an equilibrium position. The melt–gas interface is higher because of the growth angle, which is the angle formed between the melt–gas interface and the velocity vector of the triple-phase line in a frame of reference moving with the growing solid.[1] For a static problem, considering the balance of hydrostatic pressure and surface tension, the depth of the triple-phase line, $d_{TPL}$, is $d_{TPL,0} = 1.04$ mm (see Appendix A.1 of [27]). The other dimensions in Fig. 1 are $w_1 = 0.5$ mm, $w_2 = 1.5$ mm, $\alpha = 45°$, $w = 33.5$ mm, $h = 2$ mm, and $h_c = 4.6$ mm. The corners on both sides of the jet slot at $|x| = w_s/2$, $w_s/2 + w_1$, $w_s/2 + w_1 + w_2$ and $w/2$, were filleted with radii of 0.05, 0.2, 0.5, and 1 mm respectively.

#### 2.1.1. Governing equations

Steady energy conservation was solved in all three phases assuming constant specific heats and thermal conductivities and negligible viscous dissipation and compressibility effects as

$$\nabla \cdot (\rho_i c_i T_i \vec{u}_i - k_i \nabla T_i) = 0, \tag{1}$$

where subscript $i \in \{s, l, g\}$ designates solid, liquid, and gas; $\rho$ is density; $c$ is specific heat; $T$ is temperature; $\vec{u}$ is velocity; and $k$ is thermal conductivity. Convection was included in the solid because of the rigid horizontal translation.

For the melt and gas, the continuity and the Navier–Stokes equations for a Newtonian fluid were also solved as

$$\nabla \cdot \left(\rho_i \vec{u}_i\right) = 0, \tag{2}$$

$$\nabla \cdot \left(\rho_i \vec{u}_i \vec{u}_i\right) = -\nabla p_i + \nabla \cdot \boldsymbol{\tau_i} + \rho_i \vec{g}, \tag{3}$$

where $p$ is pressure; $\boldsymbol{\tau_i} = \mu_i \left(\nabla \vec{u}_i + (\nabla \vec{u}_i)^T\right)$ is the stress tensor with $\mu$ denoting dynamics viscosity; and $\vec{g}$ is the gravitational acceleration.

[1] Equivalently, growth angle can be defined as the angle between the tangents to solid–gas and melt–gas interfaces at the triple-phase line. The growth angle condition defines the growth direction of the triple-phase line during solidification. However, this condition does not apply to a melting or non-solidifying solid [30,31] (back-melting can happen in unsteady HRG as shown in Ref. [27]).

**Table 1**
The thermophysical properties used in simulations.

| Parameter | $i = s$ | $i = l$ | $i = g$ | Units |
|---|---|---|---|---|
| $\rho_i$ | 2530 [32] | 2530 [32] | $\frac{P_{atm}}{R_{He}T}$ [a] | kg/m$^3$ |
| $c_i$ | 1000 [32] | 1000 [32] | $\frac{5R_{He}}{2} = 5196$ [33] | J/(kg K) |
| $k_i$ | 22 [32] | 64 [32] | 0.352 [34] | W/(m K) |
| $\mu_i$ | – | $7 \times 10^{-4}$ [32] | $4.46 \times 10^{-5}$ [35] | kg/(m s) |

[a] $R_{He}$ is the helium gas constant.

The melt density was assumed constant to avoid buoyancy-induced flow instabilities discussed in [27]. This allowed steady solutions to be obtained. The helium gas was assumed to be calorically perfect. The physical properties are given in Table 1 where the gas thermal conductivity was evaluated at the film temperature $\frac{T_c+T_m}{2}$ where $T_m = 1685$ K is the equilibrium melting temperature and $T_c = 300$ K is the cold jet temperature at the helium inflow slot.

#### 2.1.2. Interface and boundary conditions

At the solid–melt interface, conservation of mass and energy were imposed. As solid and liquid densities were assumed equal, conservation of mass reduces to a Dirichlet boundary condition that sets the melt velocity equal to the solid sheet pull speed, $u_p$. Conservation of energy was imposed as

$$-k_s \nabla T_s \cdot \hat{n}_s - k_l \nabla T_l \cdot \hat{n}_l = \rho_s L_f \vec{u}_s \cdot \hat{n}_s, \tag{4}$$

where $\hat{n}_i$ denotes the outward unit normal vectors and the latent heat of fusion, $L_f$, is given in Table 2.

In addition, the solidification kinetics model of Ref. [36] was used to relate growth rate and degree of supercooling as

$$\Delta T = K(\Delta T, \theta_m) V_g, \tag{5}$$

where $K$ is the solidification kinetics coefficient; $\Delta T = T_m - T$ is the degree of supercooling; $\theta_m$ is the misalignment angle from the direction of the (111) facet formed at the triple-phase line; and $V_g$ is the growth rate. Assuming [011] and [100] directions to be respectively aligned with negative $x$ and positive $y$ directions, the (111) facet would be at an angle of 55° clockwise from positive $x$ direction [37]. It was assumed that the degree of supercooling at the triple-phase line is determined by two-dimensional nucleation kinetics with its coefficient $K_{2DN} = B_{2DN}^{-1} e^{\frac{A_{2DN}}{\Delta T}} \Delta T$ where $A_{2DN}$ and $B_{2DN}$ are constants given in Table 2. Along the rest of the solid–melt interface $K = \left(K_{step}^4 + K_{rough}^4\right)^{1/4}$. $K_{step} = \frac{10 K_{SN}}{|\sin \theta_m|}$ is the coefficient of step propagation kinetics where the constant of step nucleation $K_{SN}$ given in Table 2 was multiplied by 10 to avoid convergence issues, which as shown in [28] does not change the results significantly. $K_{rough}$, also given in Table 2, is the

**Table 2**
The solidification kinetics and interface parameters used in simulations.

| Parameter | Value | Unit |
|---|---|---|
| $A_{2DN}$ | 140 [36] | K |
| $B_{2DN}$ | $1.5\times10^{10}$ [36] | m/(s K) |
| $K_{rough}$ | 1/0.122 [38] | K s/m |
| $K_{SN}$ | 1/0.63 [39] | K s/m |
| $L_f$ | $1.8\times10^{6}$ [32] | J/kg |
| $\sigma$ | 0.735 [32] | N/m |
| $\epsilon_s$ | 0.6 [32] | – |
| $\epsilon_l$ | 0.2 [32] | – |

coefficient of roughened growth. As $\theta_m$ increases, the model transitions to roughened growth with smaller supercooling levels. To predict the dependence of the triple-phase line position on the pull speed, which is discussed in Section 3.2, it is essential to include the solidification kinetics [20].

A radiation heat flux that models the thermal radiation between the hot silicon and a cold surface at $T_c$ with a width of $2w_1$ centered at $x = 0$ and $y = h$ was specified along the solid–gas and the liquid-gas interfaces assuming the cold surface is black and the silicon surface is gray, opaque, and diffuse. The radiation heat flux, which had a secondary effect compared to the convective heat flux of helium, was specified as $q_{rad,i} = \epsilon_i\sigma_B F(x)(T_i^4 - T_c^4)$ where $\epsilon_i$ is emissivity given in Table 2, $\sigma_B = 5.678\times10^{-8}$ W/(m$^2$ K$^4$) is the Stefan–Boltzmann constant, and $F(x) = \frac{1}{2}\left(\frac{-w_1-x}{\sqrt{(-w_1-x)^2+h^2}} - \frac{w_1-x}{\sqrt{(w_1-x)^2+h^2}}\right)$ is the view factor to a finite length surface [40]. At the solid–gas interface, the gas velocity was set to be horizontal and equal to $u_p$. At the melt–gas interface, in addition to zero normal velocity, a jump in the normal stress from the gas to melt equal to $-2\sigma\kappa$ was imposed where $\sigma$ is the surface tension given in Table 2 and $\kappa$ is the mean curvature of the interface. The surface tension was assumed to be independent of temperature to avoid the Marangoni flow instabilities studied in [27].

In the melt subdomain, at the left side, a temperature of $T_m + 5$ K and a horizontal velocity profile corresponding to a fully-developed laminar channel flow with an average velocity of $u_p$ was specified as $-6\frac{y}{d}\left(1+\frac{y}{d}\right)u_p$. At the bottom of the melt, a heat flux was specified to model a heater used in HRG experiments as $q_b = q_H F_b(x_1)$ where $q_H = 16.63$ W/cm$^2$ and $F_b(x) = \frac{1}{2}\left(\frac{w_b-x}{\sqrt{(w_b-x)^2+(0.1d)^2}} - \frac{-w_b-x}{\sqrt{(-w_b-x)^2+(0.1d)^2}}\right)$ where $2w_b = 20.5$ mm is the width of the heater and $d = 13$ mm is the depth of melt from the horizontal melt–gas interface. The right side of the liquid was an outflow (zero total stress and heat flux). Similarly, at the right side of $\Omega_s$, a zero diffusive heat flux boundary condition was specified.

In the gas subdomain, outflow boundary conditions were imposed at the left and right sides by specifying zero total stress and heat flux. The inflow of helium at the slot was at $T_c$ with a vertical velocity profile corresponding to a fully-developed laminar channel flow as $-\frac{3}{2}V_s\left(1-(\frac{2x}{w_s})^2\right)$ where $V_s = 48.15$ m/s is the average velocity of jet. Thus, based on the hydraulic diameter of the slot jet, $2w_s$, and the viscosity and speed of sound at $T_c$, the Reynolds number and Mach number are respectively $Re = 119$ and $Ma = 0.047$. Therefore, the helium jet is laminar [41] and can be considered incompressible as $Ma < 0.1$. All of the walls including the top surfaces of the domain were no-slip. The interior, bottom, and 45°-sloped walls of the slot jet were at $T_c$. The vertical exterior walls of the jet injector were at $T_w = 1500$ K. Along the bottom wall of the injector, the temperature varied smoothly between $T_c$ and $T_w$. Likewise, the temperature along the top horizontal walls of the domain varied smoothly between $T_w$ and $T_m + 2$ K as detailed in [29].

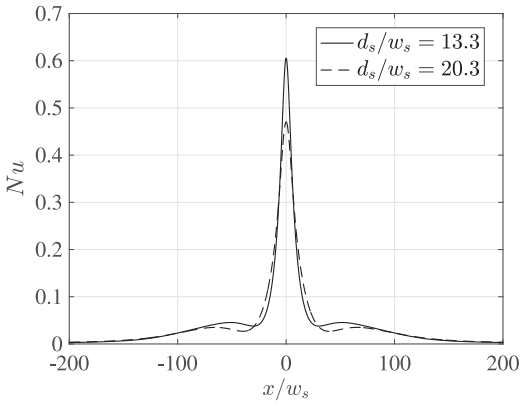


**Fig. 2.** The distributions of Nusselt number obtained from the decoupled gas simulations ($d_s/w_s = 13.3$ and $d_s/w_s = 20.3$ correspond to gas simulations for $\theta_{gr} = 0$ and $\theta_{gr} = 11°$ respectively).

### 2.2. Two-phase model

The two-phase model of the HRG only included $\Omega_s$ and $\Omega_l$ shown in Fig. 1 with the same conditions as the three-phase model imposed at the boundaries and the interface of melt and solid. The effects of $\Omega_g$ were accounted for by the boundary conditions along the solid–gas and liquid-gas interfaces. To determine these boundary conditions, the gas phase was simulated separately with the geometry and boundary conditions on the top, left and right sides kept the same as $\Omega_g$ in Section 2.1. Two simulations were performed with the bottom wall of the domain positioned at $y = 0$ and $y = -d_{TPL,0}$. These simulations correspond to the position of the triple-phase line for cases with growth angles of $\theta_{gr} = 0$ and $\theta_{gr} = 11°$ respectively. For both simulations, the bottom wall was no-slip and horizontal with a fixed temperature of $T_m$. The extracted distributions of convective heat flux, $q_{conv}$, shear stress, $\tau$, and pressure, $p$, at the bottom wall from these simulations were used as boundary conditions along the solid–gas and melt–gas interfaces. For the case with $\theta_{gr} = 11°$, the extracted shear stress and pressure distributions were imposed tangent and normal to the curved melt–gas interface, respectively. The distribution of $q_{conv}$ was converted to convection heat transfer coefficient, $h_{conv}$, where $q_{conv} = h_{conv}(T_m - T_c)$. Compared to $q_{conv}$ this gives a more accurate distribution of the heat flux when the silicon surface temperatures deviate from $T_m$.

Fig. 2 shows the Nusselt number, $Nu = \frac{h_{conv}w_s}{k_g}$, obtained from the gas-phase simulation. The results for both gas simulations are shown where $d_s$ denotes the separation distance between the slot jet exit and the solid surface. Thus, $d_s/w_s = h/w_s = 13.3$ and $d_s/w_s = (h + d_{TPL,0})/w_s = 20.3$ correspond to simulations for cases with $\theta_{gr} = 0$ and $\theta_{gr} = 11°$ respectively. Fig. 3 shows the non-dimensional distribution of shear stress and pressure in terms of the friction coefficient, $C_f = \frac{\tau}{\frac{1}{2}\rho_0 V_s^2}$, and the pressure coefficient, $C_p = \frac{p-p_{atm}}{\frac{1}{2}\rho_0 V_s^2}$, where $p_{atm} = 101.5$ kPa is the atmospheric pressure and $\rho_0 = 0.163$ kg/m$^3$ is the helium density at $T_c$ and $p_{atm}$.

The boundary conditions extracted from the gas phase simulations were applied in two-phase simulations using curves fitted to results shown in Figs. 2 and 3. These curve fits were obtained using MATLAB's Curve Fitting Toolbox. For $Nu$ and $C_p$ respectively the sum of four and three Gaussian functions of the form $a_i \exp\left(-(\frac{x-b_i}{c_i})^2\right)$ were used where $a_i$, $b_i$ and $c_i$ are the curve fit parameters. The sum of four Gaussian derivative functions of the form $a_i(x-b_i)\exp\left(-(\frac{x-b_i}{c_i})^2\right)$ was used for $C_f$. All the fitted curves were visually indistinguishable at most points from the curves shown in Figs. 2 and 3 when overlaid on the same plot. For $d_s = h + d_{TPL,0}$ curves fitted to $Nu$, $C_f$, and $C_p$ respectively had root mean squared (standard) errors of $\hat{\sigma} = \sqrt{\frac{\sum_{i=1}^{n}(y_i-\hat{y}_i)^2}{n-p}} = 2.8\times10^{-3}$,

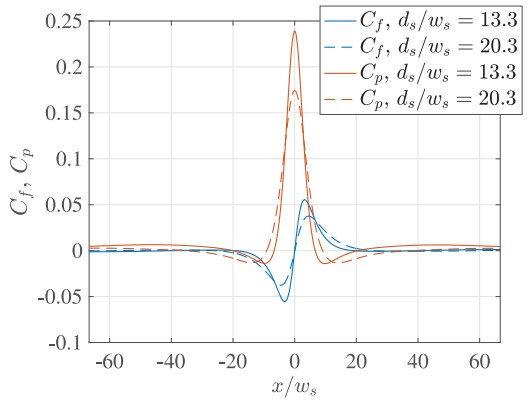


**Fig. 3.** The distributions of friction and pressure coefficients obtained from the decoupled gas simulations ($d_s/w_s = 13.3$ and $d_s/w_s = 20.3$ correspond to gas simulations for $\theta_{gr} = 0$ and $\theta_{gr} = 11°$ respectively).

$1.9 \times 10^{-4}$, and $1.2 \times 10^{-3}$ where $n$ is the number of data; $p$ is the number of curve fit parameters (9 for $C_p$ and 12 for $Nu$ and $C_f$); and $y_i$ and $\hat{y}_i$ respectively represent the data and curve fit values. The corresponding values of standard error for $d_s = h$ were $\hat{\sigma} = 3.1 \times 10^{-3}$, $2.7 \times 10^{-4}$, and $1.3 \times 10^{-3}$ respectively. All fitted curves had a coefficient of determination of $R^2 = 1.00$.

A grid convergence study was done for the simulation of the gas phase with $d_s = h + d_{TPL,0}$ using a set of three nested grids with $42 \times 10^3$, $170 \times 10^3$, and $675 \times 10^3$ degrees of freedom. Performing Richardson extrapolation for the peak value of $Nu$ (i.e. $x = 0$), the estimated error of the finest grid, which was used to obtain the curve fits, was $\epsilon_r = 0.006\%$, and the estimated order of accuracy was $p_e = 3.5$.

### 2.3. Numerical methods

To obtain solutions, a fifth-order accurate continuous high-order finite element method, *hp*-FEM, was used with a streamline upwind Petrov–Galerkin (SUPG) approach for stabilization. An arbitrary Lagrangian–Eulerian (ALE) moving mesh method was used to track interfaces and maintain mesh quality. Additionally, a local mesh adaptation scheme was utilized to obtain a uniform truncation error and enhance solution accuracy [22,42]. Also, a minimum mesh resolution was specified to prevent excessive mesh refinement near singular points. A Newton–Raphson method was applied to monolithically solve the system of equations for the temperature, and flow velocity components and the shape of all interfaces. The Jacobian matrix of the system of equations was inverted using the MUMPS solver in PETSc [43].

Obtaining converged steady solutions was challenging. The solution strategy for the three-phase model included initializing the solution with a specified convective heat flux distribution obtained from the gas simulation discussed in 2.2 with 1% of the actual gas flow rate. The specified heat flux was gradually reduced to 0 while the gas flow rate was increased. Similarly, for the two-phase simulations with shear stress imposed as a boundary condition, the shear stress was gradually increased to avoid convergence issues.

## 3. Results and discussion

### 3.1. Flow and temperature fields

Fig. 4 shows the velocity magnitude contour plot and streamlines of the three-phase simulation at $u_p = 1.5$ mm/s. Note that different color maps are used for the melt, and the gas, as well as for the gas in the zoomed-in view due to the different velocity scales of each. The main effect of the gas on the melt flow is imparting momentum. This causes melt velocity magnitudes on the order of 0.1 m/s near the surface, which are two orders of magnitude greater than $u_p$. The melt flows into the domain with a parabolic velocity profile but this is hard to see since the average inlet velocity is much smaller than the velocities induced by the gas. At the melt surface, except close to the triple-phase line, the gas induces a region of upstream flow (towards the melt inlet). This leads to a complex flow field inside the melt as shown by the streamlines. The melt flows beneath the large clockwise vortex at the inlet and then streams between two long recirculation zones towards the triple-phase line. The upper recirculation zone is counterclockwise. The second one is larger, clockwise, and encompasses smaller vortices (two of them are shown). Some of this melt flow is incorporated into the solidifying crystal and the remainder takes a tortuous path towards the outflow.

In the gas phase, the impinging jet creates two pairs of vortices, a pair near the jet exit and a pair near the silicon surface, as shown in Fig. 4. These pairs of vortices also appear in decoupled gas phase simulations discussed in Section 2.2 and their effect on enhancing the heat transfer can be seen in Fig. 2 as two local maxima in the heat flux profile at $|x|/w_s = 52$ and $|x|/w_s = 66$ for $d_s/w_s = 13.3$ and $d_s/w_s = 20.3$ respectively. Although hard to see, they also cause changes in the sign of $C_f$ in Fig. 3 at $|x|/w_s = 19$ and 40 for $d_s/w_s = 13.3$ and at $|x|/w_s = 26$ and 60 for $d_s/w_s = 20.3$. These sign changes indicate flow detachment and reattachment to the bottom wall. Note that the vortices in the gas phase simulation were symmetric. However, in Fig. 4 the vortex lying above the melt surface is smaller than the vortex above the solid surface because of the slope in the melt surface caused by the growth angle.

The temperature contours of the three-phase simulation are shown in Fig. 5. To better discern temperature variations only contours for $x > -5$ cm are shown as the temperature changes further upstream were small. Note that one color map is used for melt and solid phases and another for the gas because there is a sharp temperature gradient in the gas near the triple-phase line as it has a much smaller thermal conductivity than silicon. Similar to the velocity magnitude contours in Fig. 4, the growth angle causes asymmetry in the temperature contours near the triple-phase line.

To identify how different gas effects change the melt flow field, two-phase simulations were conducted where the gas effects were modeled by different boundary conditions as illustrated in Fig. 6a–c and compared with the three-phase flow in Fig. 6d. In Fig. 6a only the distribution of the convective heat transfer coefficient ($h_{conv}$) extracted from gas simulation with $d_s/w_s = 20.3$ was imposed (Note, that the melt in this contour plot uses a different color map). A flow resembling a channel flow is seen with velocity magnitudes on the order of $u_p$. However, when the distribution of shear stress is applied as well, a flow field much closer to the three-phase was obtained as shown in Fig. 6b. As displayed in Fig. 6c when pressure distribution was also specified along the melt–gas interface the flow field only slightly changed compared to Fig. 6b.

Fig. 7a–d show the temperature contours corresponding to flow fields illustrated in Fig. 6a–d. Fig. 7b and c agree well with the three-phase whereas the temperature contours shown in Fig. 7a are substantially different. This indicates how the disparate flow fields shown in Fig. 6a and c result in different temperature fields. At the bottom of the crucible, where a heating profile was specified to model the heater in HRG experiments, the two large vortices in Fig. 6b–d cause an upward velocity above the heater. Thus, a larger hot region is observed in Fig. 7b–d compared to Fig. 7a. Also, the melt flows induced by the gas lead to a smaller supercooled region near the triple-phase line in Fig. 7b–d compared to Fig. 7a. If buoyancy and Marangoni effects were included as well, no steady solutions could be obtained and a chaotic flow similar to that reported in our previous two-phase study [27] would ensue. In that study, the gas effects were simply modeled as a convective heat flux profile. It was shown that the Marangoni and buoyancy effects cause a chaotic flow field that leads to significant fluctuations in the position of the triple-phase line,

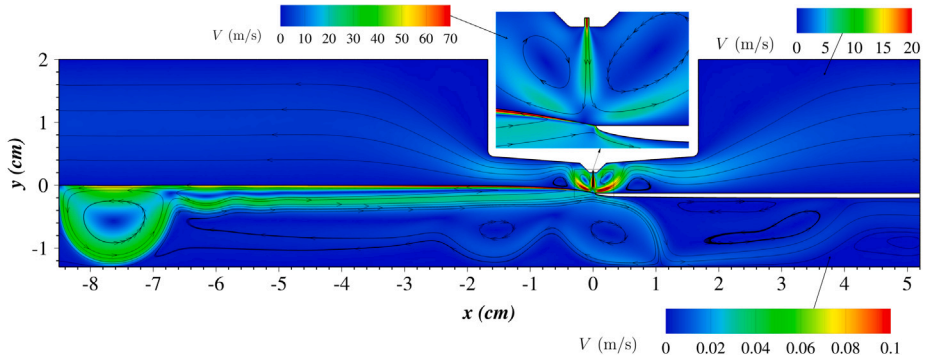


**Fig. 4.** The streamlines and velocity magnitude contours for $u_p = 1.5$ mm/s from three-phase model. Three different color maps are used for melt, gas, and its zoomed-in view. (For interpretation of the references to color in this figure legend, the reader is referred to the web version of this article.)

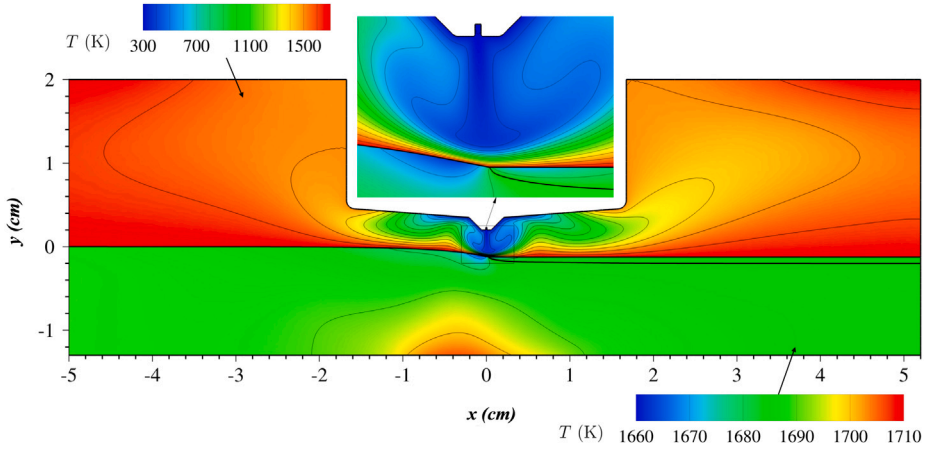


**Fig. 5.** Temperature contours for $u_p = 1.5$ mm/s from the three-phase model. The contours are 10 K apart in melt and solid and 100 K apart in the gas. (For interpretation of the references to color in this figure legend, the reader is referred to the web version of this article.)

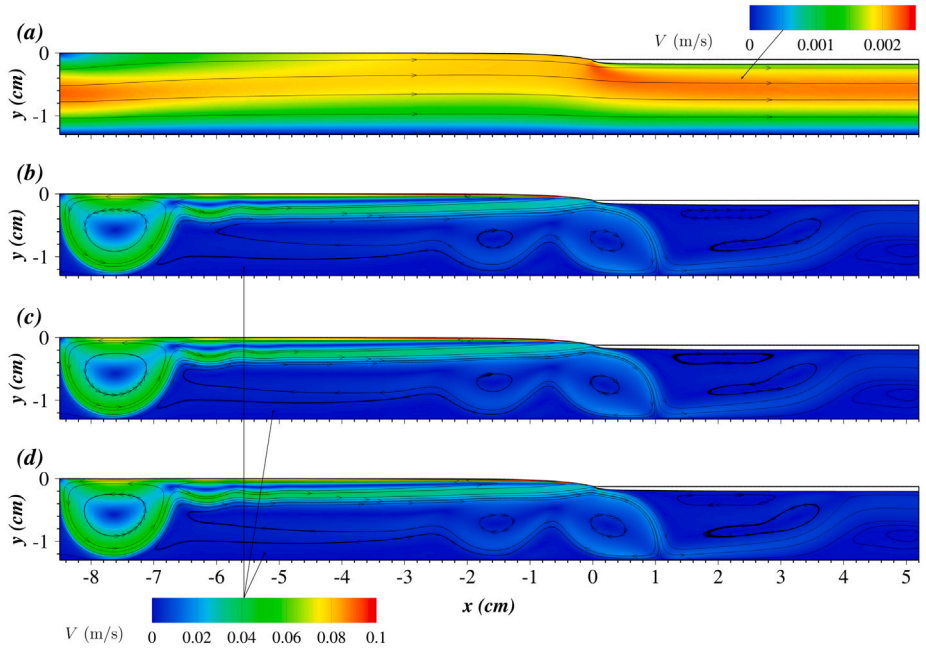


**Fig. 6.** The streamlines and velocity magnitude contours for $u_p = 1.5$ mm/s from (a) two-phase model with $h_{conv}$ specified along the melt–gas interface (b) two-phase model with $h_{conv}$ and $\tau$ specified along the melt–gas interface (c) two-phase model with $h_{conv}$, $\tau$, and $p$ specified along the melt–gas interface (d) three-phase model. Note that (a) uses a different color map than (b)–(d) for melt velocity magnitudes. (For interpretation of the references to color in this figure legend, the reader is referred to the web version of this article.)

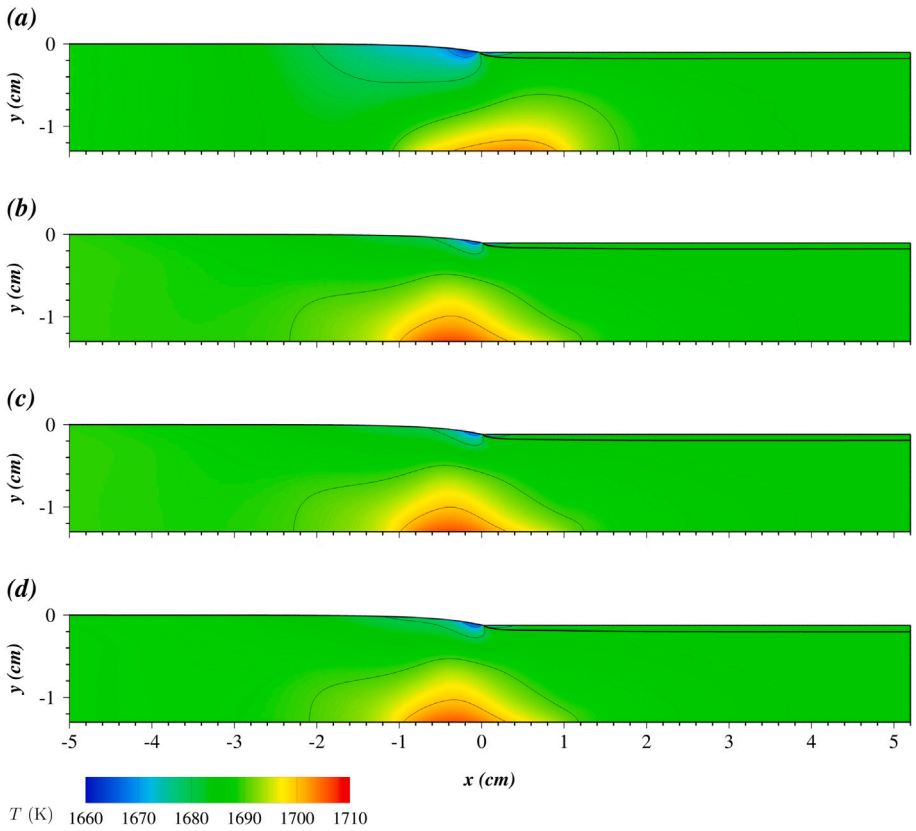


**Fig. 7.** Temperature contours for $u_p = 1.5$ mm/s from (a) the two-phase model with $h_{conv}$ specified along the melt–gas interface (b) the two-phase model with $h_{conv}$ and $\tau$ specified along the melt–gas interface (c) the two-phase model with $h_{conv}$, $\tau$, and $p$ specified along the melt–gas interface (d) the three-phase model. The contours are 10 K apart.

growth rate, and thickness. The oscillations of the triple-phase line position caused corrugations on the top surface of the solid sheet with a range of amplitudes and wavelengths. All of these phenomena were experimentally reported by Kellerman et al. [37]. The velocity magnitudes induced by the gas observed here, though smaller are still comparable to the Marangoni velocities in [27], which were found to be dominant near the surface. Thus, the gas-induced velocities when coupled with Marangoni and buoyancy effects can also play a part in the chaotic flow field reported in [27] and thus lead to triple-phase line fluctuations at higher frequencies. Such faster fluctuations may lead to smaller-wavelength surface corrugations that agree better with the experimental results of [37].

### 3.2. Pull speed response

A characteristic of HRG is its turning point behavior, which was first observed from experiments and simulations by Helenbrook et al. [20]. Because the growth rate increases with pull speed, the supercooling level at the triple-phase line increases as well (see [28] e.g.) and thus the triple-phase line moves further downstream closer to the point of maximum cooling flux (i.e. the helium jet center). As the triple-phase line position slightly moves beyond the jet center, at some pull speed solutions can no longer be obtained.

Before evaluating the pull speed response, a grid validation study was performed with $\theta_{gr} = 11°$ at $u_p = 1.5$ mm/s using sets of three nested grids to ensure that the triple-phase line positions were accurate. The baseline grids for the two-phase and three-phase simulations had similar resolutions since both used the same truncation error target for mesh adaptation. The degrees of freedom of the grids in each subdomain $i$ is given as $DOF_i$ in Table 3. Also, Table 3 shows the results of Richardson extrapolation for the horizontal and vertical positions of the triple-phase line (i.e. $x_{TPL}$ and $y_{TPL}$) in terms of the relative errors, $\epsilon_r$ and the estimated orders of accuracy, $p_e$. Note that due to singularities at the triple-phase line, the optimal order of accuracy cannot be obtained at the triple-phase line [26,29,44]. In the following calculations, meshes comparable to the coarsest meshes in Table 3 were used so the uncertainties are within 0.2% for $x_{TPL}$ and 0.03% for $y_{TPL}$.

The turning point behavior of the horizontal position of the triple-phase line, $x_{TPL}$, as a function of pull speed is shown in Fig. 8a for $\theta_{gr} = 0$. There are four curves designated as two-phase that differ in how the boundary conditions along the melt–gas interface were identified. The first one shows the results when only the convective heat flux ($q_{conv}$) was imposed. The second curve was obtained when a convective heat transfer coefficient ($h_{conv}$) was used instead. The third one includes the shear stress ($\tau$) in addition to $h_{conv}$. The last one also adds the pressure distribution. Using $h_{conv}$ is more accurate as it can account for variations in heat flux when the interface temperature deviates from $T_m$. However, comparing $h_{conv}$ with $q_{conv}$ curves, shows that $x_{TPL}$ is only slightly sensitive to use of $h_{conv}$ rather than $q_{conv}$. The addition of shear stress distribution, however, significantly improves the prediction of $x_{TPL}$, whereas including the pressure distribution does not have a significant effect on the prediction of $x_{TPL}$. The two-phase models with $\tau$ and $h_{conv}$ specified agree well with the three-phase results over the entire range of pull speeds. Note that the three-phase curve terminates before the two-phase curves since getting steady solutions approaching the turning point was more challenging with the three-phase model.

For $\theta_{gr} = 11°$ shown in Fig. 8b two-phase and three-phase results deviate as the triple-phase line gets closer to $x = 0$ since the effect of the growth angle on the flow field becomes stronger as shown in Fig. 6. Remember that in the gas phase simulations used to derive the boundary conditions the bottom boundary of the domain was a horizontal wall placed at $y = 0$ and $y = -d_{TPL,0}$ for cases with $\theta_{gr} = 0$ and $\theta_{gr} = 11°$, respectively. The difference between the results of two-phase and three-phase models is less significant when the triple-phase

**Table 3**
The grid convergence study results including the degrees of freedom of meshes in each subdomain, relative errors, and the estimated orders of accuracy using Richardson extrapolation for the horizontal and vertical position of the triple-phase line.

| Model | $DOF_l$ | $DOF_s$ | $DOF_g$ | $x_{TPL}$ (mm) | $\epsilon_r$ (%) | $p_e$ | $y_{TPL}$ (mm) | $\epsilon_r$ (%) | $p_e$ |
|---|---|---|---|---|---|---|---|---|---|
| Two-phase | $8.0\times10^4$ | $4.9\times10^3$ | – | 0.15141 | 0.16 | – | −1.20102 | 0.007 | – |
| | $3.2\times10^5$ | $1.8\times10^4$ | – | 0.15123 | 0.04 | – | −1.20097 | 0.003 | – |
| | $1.3\times10^6$ | $7.2\times10^4$ | – | 0.15119 | 0.01 | – | −1.20095 | 0.001 | – |
| | ∞ | ∞ | – | 0.15118 | – | 2.1 | −1.20093 | – | 1.4 |
| Three-phase | $8.0\times10^4$ | $5.1\times10^3$ | $5.8\times10^4$ | 0.28296 | 0.18 | – | −1.25173 | 0.024 | – |
| | $3.2\times10^5$ | $1.9\times10^4$ | $2.3\times10^5$ | 0.28261 | 0.05 | – | −1.25157 | 0.012 | – |
| | $1.3\times10^6$ | $7.6\times10^4$ | $9.0\times10^5$ | 0.28251 | 0.02 | – | −1.25150 | 0.006 | – |
| | ∞ | ∞ | ∞ | 0.28246 | – | 1.7 | −1.25143 | – | 1.0 |

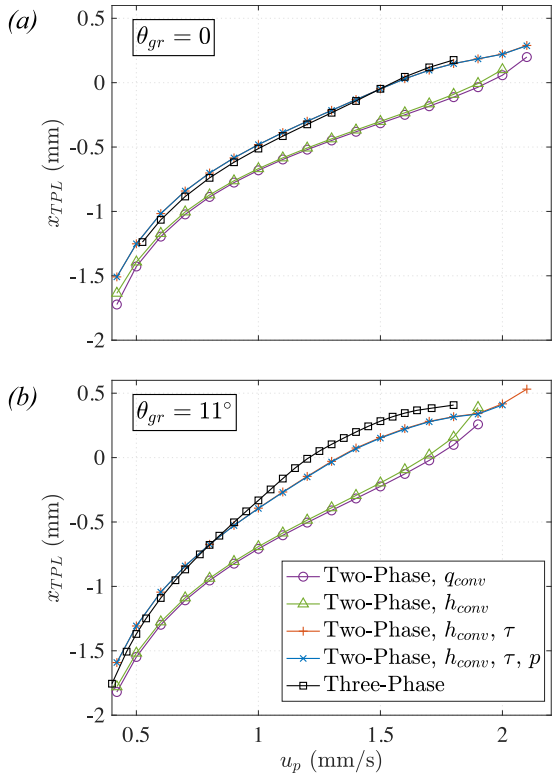


**Fig. 8.** The horizontal position of the triple-phase line as a function of pull speed from the three-phase and two-phase models with different boundary conditions along the melt–gas interface for (a) growth angle of 0 (b) growth angle of 11°. The boundary conditions specified along the melt–gas interface for two-phase models included distributions of convective heat flux ($q_{conv}$), convective heat transfer coefficient ($h_{conv}$), shear stress ($\tau$), and pressure ($p$).

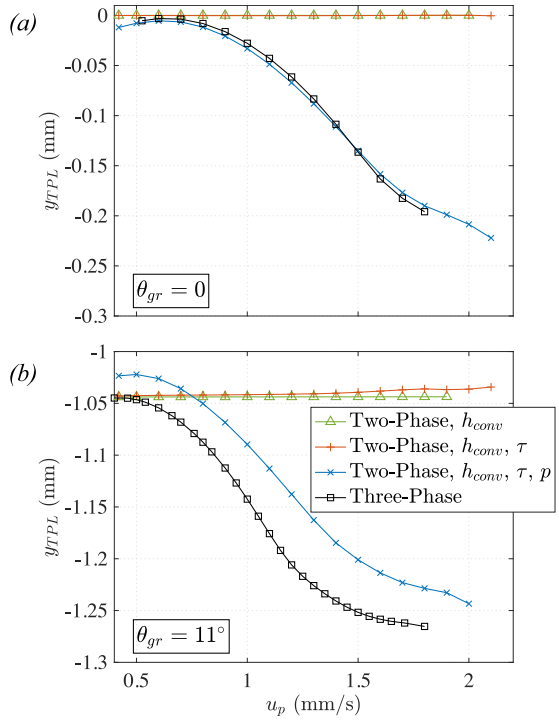


**Fig. 9.** The vertical position of triple-phase line as a function of pull speed from the three-phase and the two-phase model with different boundary conditions along the melt–gas interface for (a) growth angle of 0 (b) growth angle of 11°. The boundary conditions specified along the melt–gas interface for two-phase models included distributions of convective heat transfer coefficient ($h_{conv}$), shear stress ($\tau$), and pressure ($p$).

line is well upstream of the jet center. For the same reason, at lower pull speeds the differences between flow and temperature fields seen in Figs. 6c and d and 7c and d were smaller, and smaller yet when $\theta_{gr} = 0$.

### 3.3. Pressure effect

The vertical position of the triple-phase line, $y_{TPL}$, in the three-phase simulations also changed with the pull speed as shown in Fig. 9. The correct variation in $y_{TPL}$ could be obtained from two-phase simulations only when the pressure distribution was specified along the melt–gas interface. For the case with $\theta_{gr} = 0$, the two-phase curve with $h_{conv}$, $\tau$, and $p$ specified closely parallels the results of the three-phase simulation. However, for $\theta_{gr} = 11°$ as the growth angle modifies the melt–gas interface shape and thus the pressure distribution, there is a deviation between the two-phase model with specified $p$ distribution and three-phase simulations. This deviation increases at higher pull speeds as the triple-phase line moves closer to the jet center.

The variations in $y_{TPL}$ in Fig. 9a follow the changes in pressure distribution shown in Fig. 3 as the triple-phase line moves downstream (see Fig. 8). At higher pull speeds the triple-phase line gets closer to the peak of the pressure distribution and stabilizes at a lower $y_{TPL}$. Around $u_p = 1.5$ mm/s the vertical position of the triple-phase line is decreasing at the greatest rate. This is where the triple-phase line reaches the center of the jet with the maximum pressure. Also, there is a small increase in $y_{TPL}$ at lower pull speeds like $u_p = 0.6$ mm/s since the triple-phase line passes through a region with negative $C_p$ values.

Fortuitously, for $\theta_{gr} = 11°$ at lower pull speeds the $y_{TPL}$ for two-phase models without a specified pressure closely matches that of the three-phase simulation and the triple phase line moves upward after applying $p$. The upward movement indicates a negative average pressure along the interface. Again, this is because triple-phase line at lower pull speeds stabilizes upstream of the jet center where a vortex exists and causes negative pressures (see Figs. 3 and 8b). Also, remember that due to the growth angle, the melt–gas interface in the three-phase simulation was closer to the impinging jet than the decoupled gas simulation used to extract the boundary conditions with its bottom horizontal wall placed at $y = -d_{TPL,0}$. Thus, compared to

the two-phase model with specified $p$, the three-phase model had an average higher pressure along the melt–gas interface and pushed $y_{TPL}$ to lower values.

Variations in $y_{TPL}$ with pull speed are more than 200 μm, which is on the order of a sheet thickness and is large compared to the length of the (111) facet. Thus, gas pressure effects in an unsteady HRG with buoyancy and Marangoni effects can be important impacting $y_{TPL}$ fluctuations and corrugations on the solid surface [27].

## 4. Conclusions

Gas effects on the HRG of silicon were investigated where the latent heat of fusion is mainly removed from the melt through convection by a cold jet. This was done by comparing three-phase (solid, melt, and gas) and two-phase (solid and melt) simulations with different boundary conditions specified along the melt–gas interface. The results showed that the effects of gas shear stress and pressure are important in addition to the convective heat flux. The shear stress of the gas induced velocities two orders of magnitude larger than the pull speed and drastically changed the flow and temperature fields and thus the position of the triple-phase line. Also, the gas pressure significantly changed the vertical position of the triple-phase line. Therefore, the shear stress and pressure of the gas should also be included in two-phase models of HRG in addition to the convective heat transfer coefficient. The shear stress and pressure can couple with other sources of flow instability like Marangoni and buoyancy effects and cause variations in the shape of the crystal.

The boundary conditions for heat and momentum transfer along the gas interfaces of a two-phase simulation of HRG can be obtained from a decoupled gas phase simulation. For the cases with no growth angle, specifying the distributions of the convective heat transfer coefficient, shear stress, and pressure for the two-phase model yielded triple-phase line positions that closely matched the three-phase simulations. As the location of the triple-phase line is not known a priori, the effects of growth angle on the melt–gas interface shape cannot be included in the decoupled gas phase simulation, and this caused deviations from the three-phase results. The deviations increased as the triple-phase line moved closer to the jet centerline, where the presence of growth angle had a larger effect on the heat flux, shear stress, and pressure distributions. However, even with the growth angle effects, the two-phase model with all the extracted boundary conditions stayed in reasonable agreement with the three-phase model.

## CRediT authorship contribution statement

**Nojan Bagheri-Sadeghi:** Writing – review & editing, Writing – original draft, Visualization, Validation, Software, Methodology, Investigation. **Brian T. Helenbrook:** Writing – review & editing, Supervision, Software, Resources, Project administration, Methodology, Funding acquisition, Conceptualization.

## Declaration of competing interest

The authors declare that they have no known competing financial interests or personal relationships that could have appeared to influence the work reported in this paper.

## Data availability

Data will be made available on request.

## Acknowledgments

This material is based upon work supported by the National Science Foundation under Grant Nos. 1762802 and 2317674. Some of the computing for this project was performed on the ACRES cluster. We would like to thank Clarkson University and the Office of Information Technology for providing computational resources and support that contributed to these research results. Additional computational resources for this grant were provided by the National Science Foundation under Grant No. 1925596.

## References

[1] A.B. Crowley, Mathematical modelling of heat flow in Czochralski crystal pulling, IMA J. Appl. Math. 30 (2) (1983) 173–189, http://dx.doi.org/10.1093/imamat/30.2.173.

[2] A. Lipchin, R.A. Brown, Hybrid finite-volume/finite-element simulation of heat transfer and melt turbulence in Czochralski crystal growth of silicon, J. Cryst. Growth 216 (1) (2000) 192–203, http://dx.doi.org/10.1016/S0022-0248(00)00428-0.

[3] L. Liu, K. Kakimoto, Partly three-dimensional global modeling of a silicon Czochralski furnace, I. Principles, formulation and implementation of the model, Int. J. Heat Mass Transfer 48 (21) (2005) 4481–4491, http://dx.doi.org/10.1016/j.ijheatmasstransfer.2005.04.031.

[4] X. Liu, H. Harada, Y. Miyamura, X. Han, S. Nakano, S. Nishizawa, K. Kakimoto, Transient global modeling for the pulling process of Czochralski silicon crystal growth, I. Principles, formulation, and implementation of the model, J. Cryst. Growth 532 (2020) 125405, http://dx.doi.org/10.1016/j.jcrysgro.2019.125405.

[5] C.E. Chang, W.R. Wilcox, Analysis of surface tension driven flow in floating zone melting, Int. J. Heat Mass Transfer 19 (4) (1976) 355–366, http://dx.doi.org/10.1016/0017-9310(76)90091-0.

[6] J.L. Duranceau, R.A. Brown, Thermal-capillary analysis of small-scale floating zones: Steady-state calculations, J. Cryst. Growth 75 (2) (1986) 367–389, http://dx.doi.org/10.1016/0022-0248(86)90051-5.

[7] C. Lan, S. Kou, Heat transfer, fluid flow and interface shapes in floating-zone crystal growth, J. Cryst. Growth 108 (1) (1991) 351–366, http://dx.doi.org/10.1016/0022-0248(91)90383-G.

[8] C. Lan, J. Chian, Three-dimensional simulation of Marangoni flow and interfaces in floating-zone silicon crystal growth, J. Cryst. Growth 230 (1) (2001) 172–180, http://dx.doi.org/10.1016/S0022-0248(01)01328-8.

[9] J. Derby, R. Brown, Thermal-capillary analysis of czochralski and liquid encapsulated czochralski crystal growth: I. Simulation, J. Cryst. Growth 74 (3) (1986) 605–624, http://dx.doi.org/10.1016/0022-0248(86)90208-3.

[10] A. Virzi, Computer modelling of heat transfer in Czochralski silicon crystal growth, J. Cryst. Growth 112 (4) (1991) 699–722, http://dx.doi.org/10.1016/0022-0248(91)90126-P.

[11] H. Zhang, V. Prasad, A multizone adaptive process model for low and high pressure crystal growth, J. Cryst. Growth 155 (1) (1995) 47–65, http://dx.doi.org/10.1016/0022-0248(95)00257-X.

[12] H. Zhang, V. Prasad, D. Bliss, Modeling of high pressure, liquid-encapsulated Czochralski growth of InP crystals, J. Cryst. Growth 169 (2) (1996) 250–260, http://dx.doi.org/10.1016/S0022-0248(96)00306-5.

[13] S.S. Dossa, J.J. Derby, Modeling optical floating zone crystal growth in a high-pressure, single-lamp furnace, J. Cryst. Growth 591 (2022) 126723, http://dx.doi.org/10.1016/j.jcrysgro.2022.126723.

[14] V. Kalaev, I. Evstratov, Y. Makarov, Gas flow effect on global heat transport and melt convection in Czochralski silicon growth, J. Cryst. Growth 249 (1) (2003) 87–99, http://dx.doi.org/10.1016/S0022-0248(02)02109-7.

[15] D.E. Bornside, R.A. Brown, T. Fujiwara, H. Fujiwara, T. Kubo, The effects of gas-phase convection on carbon contamination of Czochralski-grown silicon, J. Electrochem. Soc. 142 (8) (1995) 2790, http://dx.doi.org/10.1149/1.2050094.

[16] B. Kudo, Improvements in the horizontal ribbon growth technique for single crystal silicon, J. Cryst. Growth 50 (1) (1980) 247–259, http://dx.doi.org/10.1016/0022-0248(80)90248-1.

[17] P. Daggolu, A. Yeckel, C.E. Bleil, J.J. Derby, Thermal-capillary analysis of the horizontal ribbon growth of silicon crystals, J. Cryst. Growth 355 (1) (2012) 129–139, http://dx.doi.org/10.1016/j.jcrysgro.2012.06.055.

[18] P. Daggolu, A. Yeckel, C.E. Bleil, J.J. Derby, Stability limits for the horizontal ribbon growth of silicon crystals, J. Cryst. Growth 363 (2013) 132–140, http://dx.doi.org/10.1016/j.jcrysgro.2012.10.024.

[19] P. Daggolu, A. Yeckel, J.J. Derby, An analysis of segregation during horizontal ribbon growth of silicon, J. Cryst. Growth 390 (2014) 80–87, http://dx.doi.org/10.1016/j.jcrysgro.2013.12.021.

[20] B.T. Helenbrook, P. Kellerman, F. Carlson, N. Desai, D. Sun, Experimental and numerical investigation of the horizontal ribbon growth process, J. Cryst. Growth 453 (2016) 163–172, http://dx.doi.org/10.1016/j.jcrysgro.2016.08.034.

[21] B.T. Helenbrook, N.S. Barlow, Spatial–temporal stability analysis of faceted growth with application to horizontal ribbon growth, J. Cryst. Growth 454 (2016) 35–44, http://dx.doi.org/10.1016/j.jcrysgro.2016.08.052.
[22] B. Helenbrook, J. Hrdina, High-order adaptive arbitrary-Lagrangian–Eulerian (ALE) simulations of solidification, Comput. & Fluids 167 (2018) 40–50, http://dx.doi.org/10.1016/j.compfluid.2018.02.028.
[23] T. Sun, J. Ding, C. Jiang, J. Xu, N. Yuan, Simulating the horizontal growth process of silicon ribbon, AIP Adv. 8 (8) (2018) 085307, http://dx.doi.org/10.1063/1.4996832.
[24] A. Pirnia, B.T. Helenbrook, Analysis of faceted solidification in the horizontal ribbon growth crystallization process, J. Cryst. Growth 555 (2021) 125958, http://dx.doi.org/10.1016/j.jcrysgro.2020.125958.
[25] E.P. Noronha, B.E. Ydstie, Active cooling design for horizontal ribbon growth, in: 2021 IEEE 48th Photovoltaic Specialists Conference, PVSC, 2021, pp. 0557–0559, http://dx.doi.org/10.1109/PVSC43889.2021.9518871.
[26] A. Pirnia, B.T. Helenbrook, Physics of double faceted crystal growth in solidification processes, J. Cryst. Growth 582 (2022) 126517, http://dx.doi.org/10.1016/j.jcrysgro.2022.126517.
[27] N. Bagheri-Sadeghi, B.T. Helenbrook, Buoyancy and Marangoni effects on horizontal ribbon growth, J. Cryst. Growth 596 (2022) 126822, http://dx.doi.org/10.1016/j.jcrysgro.2022.126822.
[28] N. Bagheri-Sadeghi, V.A. Fabiyi, B.T. Helenbrook, E. Paek, Sensitivity of horizontal ribbon growth to solidification kinetics, J. Cryst. Growth 603 (2023) 127038, http://dx.doi.org/10.1016/j.jcrysgro.2022.127038.
[29] N. Bagheri-Sadeghi, B.T. Helenbrook, Effects of the inert phase on solidification near a triple-phase line, J. Cryst. Growth 625 (2024) 127438, http://dx.doi.org/10.1016/j.jcrysgro.2023.127438.
[30] N. Eustathopoulos, B. Drevet, S. Brandon, A. Virozub, Basic principles of capillarity in relation to crystal growth, in: T. Duffar (Ed.), Crystal Growth Processes Based on Capillarity, John Wiley & Sons, 2010, pp. 1–49, http://dx.doi.org/10.1002/9781444320237.ch1, (Chapter 1).
[31] N. Van den Bogaert, F. Dupret, Simulation of back-melting in Czochralski growth, J. Cryst. Growth 166 (1) (1996) 446–451, http://dx.doi.org/10.1016/0022-0248(96)00135-2.
[32] M. Mito, T. Tsukada, M. Hozawa, C. Yokoyama, Y.-R. Li, N. Imaishi, Sensitivity analyses of the thermophysical properties of silicon melt and crystal, Meas. Sci. Technol. 16 (2) (2005) 457–466, http://dx.doi.org/10.1088/0957-0233/16/2/018.
[33] R. Bird, W. Stewart, E. Lightfoot, Transport Phenomena, second ed., Wiley, 2002.
[34] T. Bergman, T. Bergman, F. Incropera, D. DeWitt, A. Lavine, Fundamentals of Heat and Mass Transfer, seventh ed., Wiley, 2011.
[35] F. White, Fluid Mechanics, seventh ed., McGraw-Hill, 2011.
[36] O. Weinstein, S. Brandon, Dynamics of partially faceted melt/crystal interfaces I: Computational approach and single step–source calculations, J. Cryst. Growth 268 (1) (2004) 299–319, http://dx.doi.org/10.1016/j.jcrysgro.2004.04.108.
[37] P. Kellerman, B. Kernan, B.T. Helenbrook, D. Sun, F. Sinclair, F. Carlson, Floating silicon method single crystal ribbon – observations and proposed limit cycle theory, J. Cryst. Growth 451 (2016) 174–180, http://dx.doi.org/10.1016/j.jcrysgro.2016.07.012.
[38] D. Buta, M. Asta, J.J. Hoyt, Kinetic coefficient of steps at the Si(111) crystal-melt interface from molecular dynamics simulations, J. Chem. Phys. 127 (7) (2007) 074703, http://dx.doi.org/10.1063/1.2754682.
[39] V.V. Voronkov, Supercooling at the face developing on a rounded crystallization front, Sov. Phys. – Crystallogr. 17 (5) (1973) 807–813.
[40] J.R. Howell, M.P. Mengüç, R. Siegel, Thermal Radiation Heat Transfer, seventh ed., CRC Press, 2016, URL http://www.thermalradiation.net/sectionb/B-71.html.
[41] N. Zuckerman, N. Lior, Jet Impingement Heat Transfer: Physics, Correlations, and Numerical Modeling, in: Advances in Heat Transfer, vol. 39, Elsevier, 2006, pp. 565–631, http://dx.doi.org/10.1016/S0065-2717(06)39006-5.
[42] B. Helenbrook, A two-fluid spectral-element method, Comput. Methods Appl. Mech. Engrg. 191 (3) (2001) 273–294, http://dx.doi.org/10.1016/S0045-7825(01)00275-4.
[43] S. Balay, S. Abhyankar, M.F. Adams, S. Benson, J. Brown, P. Brune, K. Buschelman, E.M. Constantinescu, L. Dalcin, A. Dener, V. Eijkhout, J. Faibussowitsch, W.D. Gropp, V. Hapla, T. Isaac, P. Jolivet, D. Karpeev, D. Kaushik, M.G. Knepley, F. Kong, S. Kruger, D.A. May, L.C. McInnes, R.T. Mills, L. Mitchell, T. Munson, J.E. Roman, K. Rupp, P. Sanan, J. Sarich, B.F. Smith, S. Zampini, H. Zhang, J. Zhang, PETSc/TAO Users Manual (Rev. 3.20), Argonne National Lab, 2023, http://dx.doi.org/10.2172/2205494.
[44] B.T. Helenbrook, Solidification along a wall or free surface with heat removal, J. Cryst. Growth 418 (2015) 79–85, http://dx.doi.org/10.1016/j.jcrysgro.2015.02.028.